Measurement of Water Vapor Flux Profiles in the Convective Boundary Layer with Lidar and Radar–RASS

CHRISTOPH SENFF AND JENS BÖSENBERG

Max-Planck-Institut für Meteorologie, Hamburg, Germany

GERHARD PETERS

Meteorologisches Institut der Universität Hamburg, Hamburg, Germany

(Manuscript received 13 December 1991, in final form 27 August 1992)

ABSTRACT

A remote-sensing method to retrieve vertical profiles of water vapor flux in the convective boundary layer by using a differential absorption lidar and a radar–radio acoustic sounding system is described. The system's height range presently extends from 400 to 700 m above the surface, and flux data can be sampled with a height resolution of 75 m and a time resolution of 60 s. The results of a first measurement in July 1991 under predominantly convective conditions are presented. The resolution of the remote-sensing system apparently is sufficient to resolve the major contributions to the flux in the convective mixed layer. In addition, the advantages and limitations of this method are discussed.

1. Introduction

The knowledge of vertical profiles of water vapor flux is crucial in order to understand dynamical processes in the boundary layer, especially the formation of clouds. Water vapor flux measurements over land at ground level are usually not representative of the entire boundary layer, since the fluxes in the middle and upper boundary layer are strongly influenced by entrainment processes that have no measurable effect on the surface flux. Furthermore, surface measurements are representative only for the surface conditions in a rather small upstream area. Up to now, the determination of water vapor flux profiles is based on in-situ aircraft measurements. This paper describes a ground-based active remote-sensing technique that has the advantage that vertical flux profiles can be measured simultaneously at different height levels. In addition, measurements can be repeated over long periods of time with relatively low logistic and financial effort.

The DIAL system (differential absorption lidar) of the Max-Planck-Institut für Meteorologie in Hamburg and the radar–RASS (radio acoustic sounding system) operated by the Meteorologisches Institut der Universität Hamburg have proven to be powerful tools to measure water vapor and vertical wind velocity profiles, respectively. During an experiment in July 1991, these two instruments were operated simultaneously in order to obtain vertical profiles of water vapor flux in the boundary layer. As a first example, the results of a 6-h measurement period are presented.

Corresponding author address: Dr. Christoph Senff, Max-Planck-Institut für Meteorologie, Bundesstr.55 20146 Hamburg, Germany.

2. Experimental setup

a. DIAL system

The DIAL system of the Max-Planck-Institut consists of two pulsed, narrowband tunable dye lasers, one of which is tuned to the center wavelength of a suitable water vapor absorption line in the 729-nm region, while the other is tuned off line. To tune the on-line laser with high precision and to monitor its stability, a photoacoustic cell filled with water vapor at low pressure is used. The spectral distribution of the on-line laser is recorded with a high-resolution Fizeau interferometer. On- and off-line laser beams, which have orthogonal polarization, are combined in a Glan–Thompson prism, then expanded and emitted vertically into the atmosphere. The time lag between the on- and off-line laser pulses is 200 μs, which guarantees that the backscatter and extinction properties of the atmosphere along the laser beam path are essentially the same for on- and off-line pulse. The DIAL receiver for the elastically backscattered signals consists of a 28-cm telescope, a photomultiplier and a 12-bit, 20-MHz transient recorder. To reduce background light the return signals are passed through an 8-nm filter. The whole DIAL system is built into a 6-m $\times$ 2.5-m container. The most important technical details are listed in Table 1. More detailed information about the technical as-

pects of the DIAL system can be found in Bösenberg (1991).

b. Radar–RASS

The radar–RASS is operated in FM–CW (frequency modulated–continuous wave) mode (Chadwick and Strauch 1979) at a center frequency of 1235 MHz and is used to measure the sound velocity parallel to a vertically pointing beam. The principle of RASS operation of an FM–CW radar is described by Peters et al. (1988), and further details of the measuring system can be found in a separate paper (Peters and Kirtzel 1994). Table 2 lists the most important technical details of the radar–RASS system. The sound velocity is derived from radar echoes scattered by acoustic waves that are generated by a sound source located close to the radar. The sound source, which is mounted on a cart, can be moved around the radar antennas, and its radial distance can be adjusted to compensate for the drift of the sound waves caused by horizontal wind.

Usually, the temperature is retrieved from the sound velocity measured by a RASS. In this experiment the sound velocity fluctuations have been used to determine vertical wind velocity fluctuations. The disadvantage of this method as compared to clear-air radar measurements of vertical wind are the limited RASS height range and a systematic error due to the dependence of the sound velocity on temperature (see section 3). However, the advantages of using RASS to measure vertical wind fluctuations are the low system noise due to the deterministic scattering structure and the immunity from ground clutter (Peters 1990).

c. Combined setup of DIAL and radar–RASS

DIAL and radar–RASS are situated at a flat site northwest of Hamburg with the ground cover being mostly grass. The horizontal distance between the two systems amounts to about 15 m. Due to the different beam divergences of lidar ($\varphi < 0.5$ mrad) and radar ($\varphi \approx 60$ mrad), the measurement volumes of the two systems are considerably different, but the horizontal scales of the turbulent processes that are detected with these systems are much larger than the beamwidth and the separation of the two beams.

Due to an incomplete overlap between the DIAL receiver telescope's field of view and the laser beam, water vapor data can be retrieved only above 400 m. The maximum height extends well beyond the planetary boundary layer unless low optically thick clouds obstruct the laser beam. The range of the radar–RASS system is limited to about 700 m mostly due to an unavoidable drift of the sound waves caused by horizontal wind. This means that under favorable conditions—that is, no low clouds and sufficiently strong return signals—the usable range of the combined DIAL–radar system extends from about 400 to 700 m above the surface.

The height and time resolution of the radar–RASS are 75 m and 10 s, respectively. The lidar return signals are recorded with a spatial resolution of 7.5 m and a time resolution of 10 s. Since the relation between water vapor concentration and measured DIAL data is nonlinear, the signal-to-noise ratio has to be larger than ten to keep the systematic errors below an acceptable limit (Bösenberg and Theopold 1988). Therefore, the DIAL data are averaged over 75 m in height and 60 s timewise, which determines the time resolution of the combined system.

To complement the lidar and radar measurements radiosondes can be launched every 2–3 h.

3. Data evaluation

The details of the DIAL and radar–RASS data analysis are described elsewhere (Cahen et al. 1982; Zuev et al. 1983; Peters et al. 1988). Here, the focus will be on processing the data to obtain water vapor and vertical wind fluctuations, which are needed to calculate the turbulent water vapor flux.

To retrieve water vapor density profiles from the DIAL data, the standard DIAL equation (Schotland 1974) has been extended. First, the pressure and temperature dependence of the absorption line parameters are considered (Cahen et al. 1982). The pressure and temperature profiles are obtained from the radiosonde ascents at the measurement site. To calculate the effective absorption cross section correctly, the emitted on-line laser spectrum is recorded with a high-resolution Fizeau interferometer, and the Doppler broadening of the Rayleigh backscattered part of the received spectrum is taken into account (Ansmann and Bösenberg 1987). In addition, the modified DIAL equation corrects for the spectral impurity of the on-line laser, that is, the amount of broadband amplified sponta-

TABLE 1. DIAL system parameters.

Transmitters (2 Excimer pumped dye lasers)	
Output energy	35 mJ
Bandwidth FWHM	1.5 pm
Spectral impurity	<2%
Repetition rate	12 Hz typical, 24 Hz tested
Beam dimensions	2 mm × 2 mm
Beam divergence (prior to expansion)	1.5 mrad
Beam expansion	×15 (optionally ×25 or ×35)
Bandwidth measurement (Fizeau interferometer)	
Resolution of readout	0.1 pm
Optical resolution	0.8 pm
Receiving optics	
Schmidt Cassegrain telescope, diameter	0.28 m
Newtonian telescope, diameter	0.5 m
Distance transmitter–receiver	0.3 m (3.0 m optionally)
Filter bandwidth	8 nm (0.6 nm optionally)

TABLE 2. RASS system parameters.

Radar	
Radar type	FM-CW with separate transmit and receiving antenna
Antenna type	Steerable phased array with 4 × 4 elements
Aperture	1.6 m × 1.6 m
Transmitted power	50 W
Center frequency	1235 MHz
Bandwidth	2 MHz (adjustable according to range resolution)
Sweep repetition rate	100 Hz (adjustable according to Nyquist velocity)
Acoustic source	
Transmitted power	10 W
Bandwidth	100 Hz (sweep repetition rate)
Center frequency	Manually adjustable to f_a (Hz) = 165.05 $[T(\mathrm{K})]^{1/2}$, where f_a is the acoustic frequency and T the mean temperature.

neous emission (ASE) (Bösenberg 1991). The ASE level is determined from an additional measurement with an absorption line of different strength.

The time series of water vapor density $q(t)$ measured at different heights are high-pass filtered to remove long-term variations that do not contribute to the turbulent water vapor flux. The filtering is performed by subtracting a moving average over a suitable time period Δt from each value $q(t_i)$, that is, the water vapor fluctuations $q'(t_i)$ are calculated according to

$$q'(t_i) = q(t_i) - \bar{q}\left(t_i - \frac{\Delta t}{2}, t_i + \frac{\Delta t}{2}\right). \quad (1)$$

The velocity c_s of the sound waves is retrieved from the frequency spectrum of the RASS return signal. Here, c_s is the sum of the sound velocity c_a relative to the medium and the vertical wind speed w

$$c_s = c_a + w. \quad (2)$$

The same relationship holds for the fluctuations

$$c_s' = c_a' + w', \quad (3)$$

which are derived from the original c_s data by applying a high-pass filter in the same manner as for the water vapor data.

The covariance of sound velocity with water vapor yields

$$\overline{c_s'q'} = \overline{c_a'q'} + \overline{w'q'}, \quad (4)$$

which deviates from the water vapor flux $\overline{w'q'}$ by $\overline{c_a'q'}$. Here, c_a' can be expressed as

$$c_a' = \frac{\partial c_a}{\partial T} T' + \frac{\partial c_a}{\partial q} q', \quad (5)$$

where T' and q' are the fluctuations of temperature and humidity, respectively. With the relation for the sound velocity c_a in moist air (Harris 1971)

$$c_a = \left[R_d \gamma_d T\left(1 + 0.326 \frac{R_v}{p} qT\right)\right]^{1/2}, \quad (6)$$

in which R_d and R_v are the gas constants for dry air and water vapor, γ_d is the ratio of specific heats of dry air and p, q, and T are air pressure, humidity and dry temperature, $\overline{c_a'q'}$ can be written as

$$\overline{c_a'q'} = 0.5 \frac{\bar{c}_a}{\bar{T}} \overline{T'q'} + 0.16 \frac{R_v \bar{c}_a \bar{T}}{\bar{p}} \overline{q'^2} \quad (7)$$

with the mean values $\bar{c}_a$, $\bar{p}$, and $\bar{T}$.

Since the water vapor flux is calculated using water vapor density data, errors due to density fluctuations have to be taken into account. As described in Webb et al. (1980) the measured flux $\overline{w'q'}$ is corrected according to

$$\overline{w'q'}_{\mathrm{corr}} = \left(1 + \frac{M_a}{M_v} \frac{\bar{q}}{\bar{\rho}_d}\right)\left(\overline{w'q'} + \frac{\bar{q}}{\bar{T}} \overline{w'T'}\right), \quad (8)$$

where M_a and M_v are the molecular weights of air and water vapor, $\bar{q}$ and $\bar{\rho}_d$ are the average water vapor and dry-air densities, and $\overline{w'T'}$ is the heat flux. Inserting (4) and (7) into (8) yields

$$\overline{w'q'}_{\mathrm{corr}} = \underbrace{\left(1 + \frac{M_a}{M_v} \frac{\bar{q}}{\bar{p}} R_d \bar{T}\right)}_{1}\left(\overline{c_s'q'} - \underbrace{0.5 \frac{\bar{c}_a}{\bar{T}} \overline{T'q'}}_{2}\right.$$

$$\left. - \underbrace{0.16 \frac{R_v \bar{c}_a \bar{T}}{\bar{p}} \overline{q'^2}}_{3} + \underbrace{\frac{\bar{q}}{\bar{T}} \overline{w'T'}}_{4}\right). \quad (9)$$

The correction terms 1 and 3 can be evaluated, since the average water vapor density $\bar{q}$ and its variance $\overline{q'^2}$ are known from the lidar measurements and $\bar{c}_a$ is available from the radar measurements. Here, $\bar{p}$ and $\bar{T}$ are obtained from radiosonde measurements, but data calculated from surface pressure and temperature can be used as well without loosing much in accuracy. The humidity–temperature covariance and the heat flux cannot be derived from any of our measurements. So, terms 2 and 4 in (9) represent an unknown bias. Their order of magnitude can be estimated from mixed-layer similarity theory. According to Lenschow et al. (1980) the humidity–temperature covariance obeys

$$\overline{T'q'} = 1.8\left(\frac{z}{z_i}\right)^{-2/3}\left(1 - 2\frac{z}{z_i}\right)\frac{(\overline{w'T'})_s}{w_*}\frac{(\overline{w'q'})_s}{w_*}, \quad (10)$$

where z is the height above the ground, z_i the boundary-layer depth, w_* the convective velocity scale, $(\overline{w'T'})_s$ the surface heat flux, and $(\overline{w'q'})_s$ the surface water vapor flux. The heat flux in a convective boundary layer usually decreases linearly with height according to

$$(\overline{w'T'}) = (\overline{w'T'})_s\left[1 + (R - 1)\frac{z}{z_i}\right], \quad (11)$$

with R being the ratio of entrainment and surface heat flux. A typical value of R in a well-mixed boundary layer is −0.2 (Stull 1976). Thus, the systematic error $\Delta_{\overline{w'q'}}$ of the measured water vapor flux due to terms 1, 2, and 4 in (9) can be written as

$$\Delta_{\overline{w'q'}} = \left(1 + \frac{M_a}{M_v}\frac{\bar{q}}{\bar{p}} R_d \bar{T}\right)\left(\frac{\bar{q}}{\bar{T}}\overline{w'T'} - 0.5\,\frac{\bar{c}_a}{\bar{T}}\overline{T'q'}\right)$$

$$= \left(1 + \frac{M_a}{M_v}\frac{\bar{q}}{\bar{p}} R_d \bar{T}\right)\left[\frac{\bar{q}}{\bar{T}}(\overline{w'T'})_s\left(1 - 1.2\frac{z}{z_i}\right) - 0.9\,\frac{\bar{c}_a}{\bar{T}}\left(\frac{z}{z_i}\right)^{-2/3}\left(1 - 2\frac{z}{z_i}\right)\frac{(\overline{w'T'})_s}{w_*}\frac{(\overline{w'q'})_s}{w_*}\right]$$

$$\approx \left(1 + \frac{M_a}{M_v}\frac{\bar{q}}{\bar{p}} R_d \bar{T}\right)\left[\frac{\bar{q}}{\bar{T}}(\overline{w'T'})_s\left(1 - 1.2\,\frac{z}{z_i}\right)\right.$$

$$\left. - 0.9\,(R_d\gamma_d)^{1/2} g^{-2/3} z^{-2/3}\left(1 - 2\frac{z}{z_i}\right)\bar{T}^{1/6}(\overline{w'T'})_s^{1/3}(\overline{w'q'})_s\right], \quad (12)$$

where g is the constant of gravity. In the last step leading to (12), it is assumed that $(\overline{w'T'_v})_s \approx (\overline{w'T'})_s$. With a boundary-layer depth z_i = 1200 m, an average temperature $\bar{T}$ = 288 K, a humidity of $\bar{q}$ = 10 g m^{-3}, a pressure of $\bar{p}$ = 1013 hPa, a surface heat flux $(\overline{w'T'})_s$ = 0.2 m s^{-1} K, and a surface water vapor flux $(\overline{w'q'})_s$ = 0.15 g m^{-2} s^{-1}, the error $\Delta_{\overline{w'q'}}$ due to the unknown heat flux and humidity–temperature covariance is less than ±0.004 g m^{-2} s^{-1} in the height range of 400–700 m (Table 3). This is considered negligible compared to typical water vapor fluxes of 0.05–0.1 g m^{-2} s^{-1} in the middle of a convective boundary layer. This means that the latent heat flux E can be calculated from the water vapor density and sound velocity time series according to

$$E = L_v\,\overline{w'q'}_{\text{corr}} \approx L_v\left(1 + \frac{M_a}{M_v}\frac{\bar{q}}{\bar{p}} R_d \bar{T}\right) \times \left(\overline{c'_s q'} - 0.16\,\frac{R_v \bar{c}_a \bar{T}}{\bar{p}}\overline{q'^2}\right), \quad (13)$$

where L_v is the latent heat of vaporization of water.

The time series $q'(t)$ and $c'_s(t)$ are Fourier transformed to yield the variance spectra S_{qq} and S_{cc} and the covariance spectrum C_{qc}, which are normalized according to

$$\int_0^{f_{\max}} S_{qq}(f)\,df = \sigma_q^2, \quad \int_0^{f_{\max}} S_{cc}(f)\,df = \sigma_c^2, \quad \int_0^{f_{\max}} C_{qc}(f)\,df = \sigma_{qc}, \quad (14)$$

where σ_q^2 is the variance of the humidity, σ_c^2 the variance of the sound velocity, and σ_{qc} the covariance of humidity and sound velocity.

4. Water vapor flux measurements

As an example of water vapor flux measurements with lidar and radar–RASS, the results of measurements on 10 July 1991 are presented. Both systems were operated simultaneously and continuously for about 6 h, with only a few short interruptions to readjust the DIAL system. At upper boundary-layer levels, either the lidar return signals were not reliable due to low cumulus clouds or the radar return signals were too weak. The water vapor data below 400 m could not be used, due to a still incomplete overlap between the laser beam and the receiver telescope's field of view. So, the usable height range of the system extended from 400 to 700 m for this experiment.

a. Meteorological situation

A contour plot of the range-corrected lidar return signal from the off-line laser (Fig. 1) provides an overview of the meteorological situation. Clouds are represented by patches of strongly enhanced backscatter intensity, while the sharp decrease in backscatter intensity indicates the upper boundary of the mixed layer. When the measurement started at 1136 local time the first cumulus clouds had just begun to form with cloud-base heights at 800–900 m. The boundary-layer depth was about 1100 m, and thermal plumes extended to nearly 1700 m. During the day, due to convective processes, the cumulus cloud base as well as the boundary-layer height rose to about 1100 and 1500 m, respectively. This is confirmed by the radiosonde data (Fig. 2) taken at 1432 local time. Above 1100 m the relative humidity decreased and the atmosphere became more stable indicating the entrainment zone. The free troposphere started at about 1700 m as determined from the steep decrease in humidity. As can be seen from Fig. 1, the convection breaks down in the afternoon, the cumulus clouds dissolve, and the boundary-layer depth decreases to about 1100 m.

TABLE 3. Error in water vapor flux for different heights z according to Eq. (12).

z (m)	$\Delta_{\overline{w'q'}}$ (g m^{-2} s^{-1})
400	−0.0013
500	0.0012
600	0.0028
700	0.0040

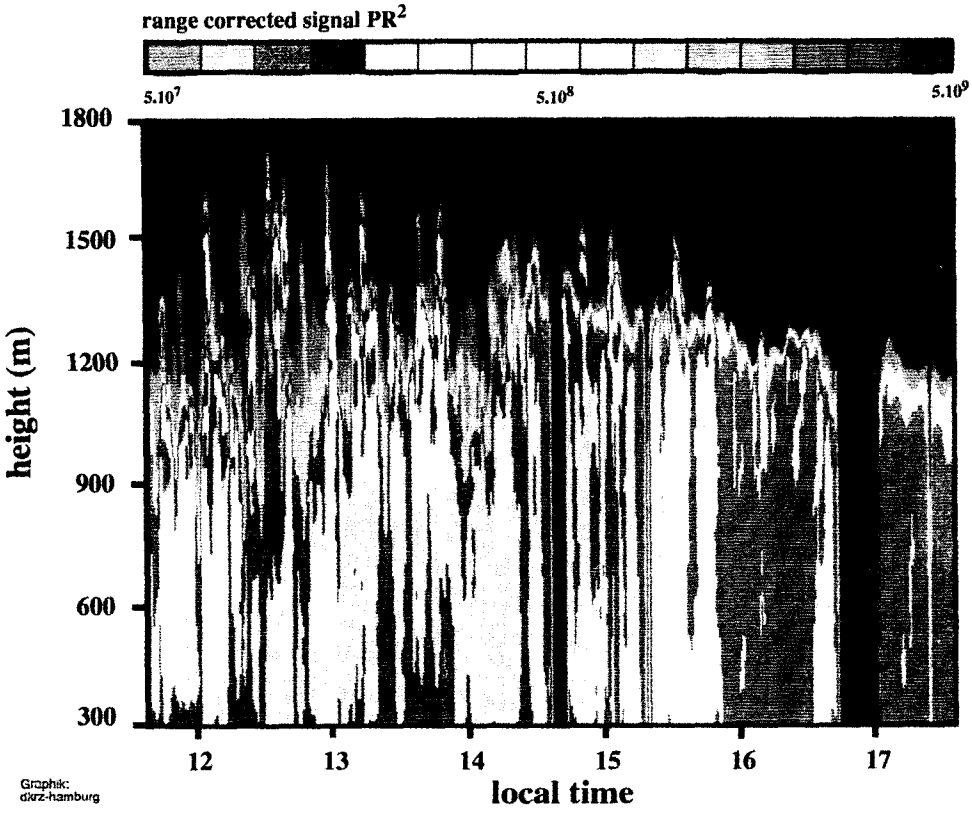

FIG. 1. Range-corrected lidar signal for offline wavelength (arbitrary units, logarithmic scale).

b. Results

The water vapor and sound velocity time series are high-pass filtered according to (1) using a filter length Δt = 30 min. The influence of the filter length on the flux was assessed by calculating the water vapor flux according to (13) for the first 3 h of the measurement from time series $q'(t)$ and $c_s'(t)$ produced by using different filter lengths. While the flux increased strongly when the filter length was changed from 10 to 30 min, the increase of the flux for filter lengths ranging from 30 to 60 min was less than 25%. To allow the evaluation

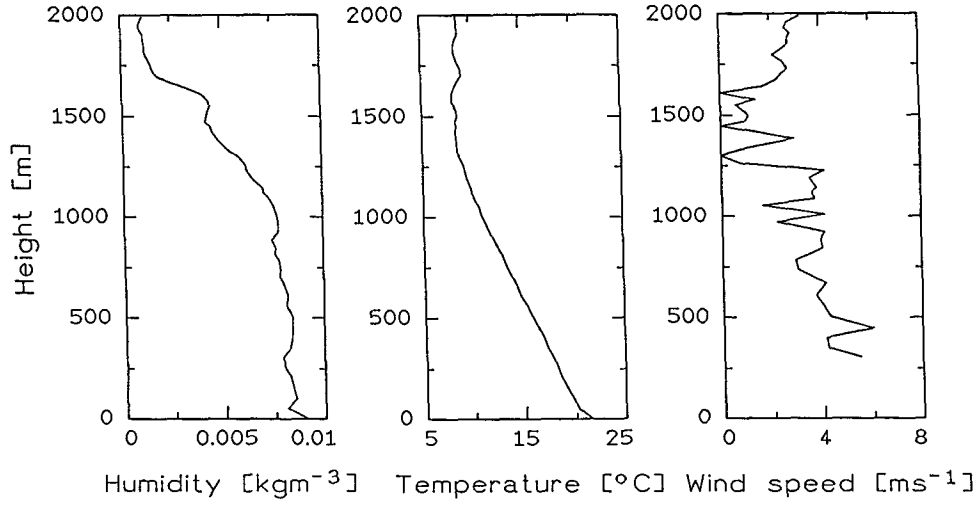

FIG. 2. Humidity, temperature, and wind speed profiles from radiosonde ascent (1432 LT).

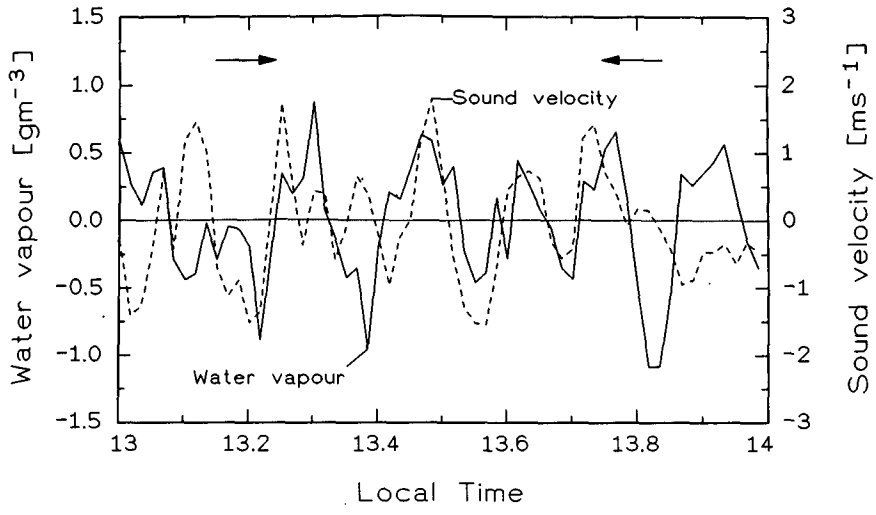

FIG. 3. Water vapor and sound velocity fluctuations at 525 m above ground level. The arrows mark a 30-min period of strong convection with cumulus clouds above the measurement site.

of periods as short as 30 min, which are chosen to represent particular meteorological conditions (e.g., with/without cumulus clouds), Δt = 30 min was selected for all water vapor flux evaluations.

Assuming the validity of Taylor's (1938) frozen-field hypothesis, a time resolution of 60 s, and a filter length of 30 min along with a 4 m s^{-1} wind means that the horizontal dimensions of the eddies that are sampled by the DIAL–RASS system range from about 500 m to 7 km.

In Fig. 3 the water vapor and sound velocity fluctuations at a height of 525 m are plotted for the 60-min time span between 1300 and 1400 local time. The water vapor fluctuations range from −1.0 to 0.9 g m^{-3}, while the sound velocity fluctuations range from about −1.6 to 1.8 m s^{-1}. For the most part, the two time series are rather closely correlated, especially during the 30-min interval marked by the two arrows, which coincides with the passage of several cumulus clouds over the measurement site. During this 30-min interval, the correlation coefficient between q' and c_s' reaches 0.54.

Figure 4 shows the power spectral density of the water vapor time series at a height of 525 m, where $\log S_{qq}(f)$ is plotted versus $\log f$. In Fig. 5 the power spectral density of the sound velocity fluctuations is plotted in the same manner at a height of 525 m as well. The solid lines in both plots indicate a decrease of the spectrum according to a −5/3 power law as predicted for the inertial subrange. At the high-frequency end, both spectra follow the −5/3 power law; there is a considerable deviation at lower frequencies. This suggests that the high-frequency portions of the power spectra are in the inertial subrange region, which, in turn, means that the contribution to the water vapor flux from frequencies larger than the Nyquist frequency

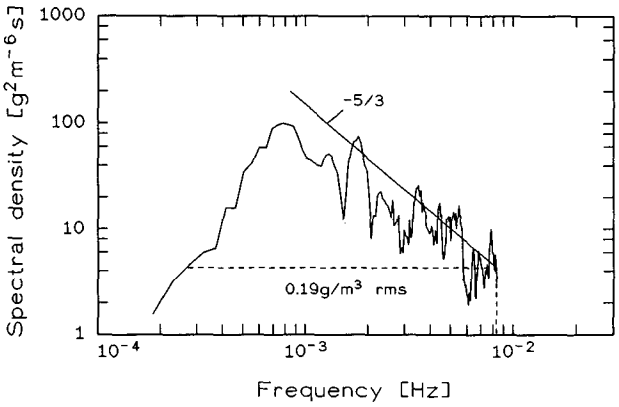

FIG. 4. Variance spectrum of humidity fluctuations (height: 525 m, time: 1136–1736 LT).

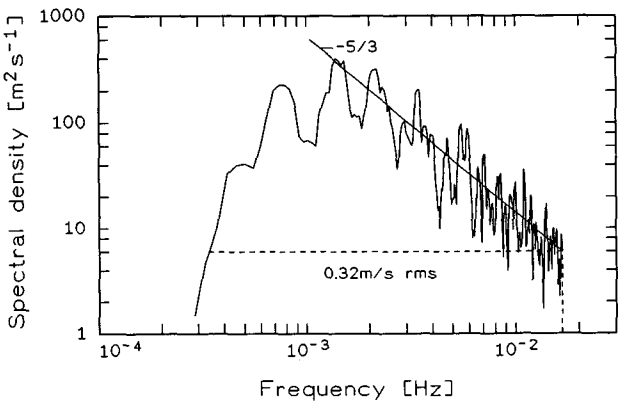

FIG. 5. Variance spectrum of sound velocity fluctuations (height: 525 m, time: 1136–1736 LT).

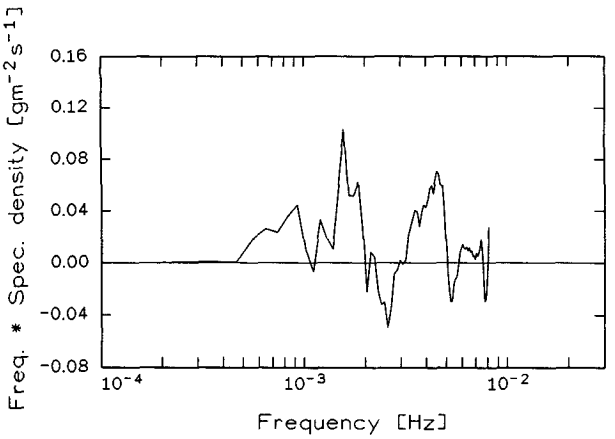

FIG. 6. Cospectrum of humidity and sound velocity fluctuations (height: 525 m, time: 1136–1436 LT).

of the DIAL–RASS system should be small compared to the flux carried by the large eddies. The covariance spectrum of water vapor and sound velocity fluctuations (Fig. 6) for the same height supports this. In Fig. 6 a plot of fC_{qc} versus $\log f$ is shown, which preserves area and thus gives realistic weight to high frequencies. It can clearly be seen from Fig. 6 that the contribution to the covariance tends to zero for frequencies above about 5×10^{-3} Hz, which corresponds to a horizontal scale $\eta \approx 800$ m.

The accuracies of the covariance $\overline{c_s'q'}$ and the humidity variance $\overline{q'^2}$ are influenced by the following three sources of error:

First, a systematic error is introduced by the somewhat arbitrary choice of the filter length Δt. The water vapor flux calculated according to (13) increases by about 25% when a filter length of 60 min instead of 30 min is used. This is an estimate for the error due to the partitioning of the water vapor and sound velocity time series into mean and fluctuating part.

Second, variance and covariance have statistical errors due to the statistical measurement errors of q' and c_s'. The latter can be estimated from the power spectra as shown in Figs. 4 and 5 for a height of 525 m. Under the assumption that the noise spectrum is flat, the noise level is equal to the smallest significant value of the power spectral density. Then the variance corresponding to the area under the noise spectrum—indicated by the dashed lines in Figs. 4 and 5—is an upper limit for the statistical noise. This leads to rms errors of less than or equal to 0.19 g m^{-3} for the water vapor fluctuations and 0.32 m s^{-1} for the sound velocity fluctuations at a height of 525 m.

Assuming Gaussian statistics and uncorrelated errors $\Delta_{q'}$ and $\Delta_{c_s'}$, the statistical error of the product $q'c_s'$ is

$$\Delta^2_{q'c_s'} = c_s'^2\Delta^2_{q'} + q'^2\Delta^{2'}_{cs}. \tag{15}$$

The statistical error of the covariance $\overline{c_s'q'}$ averaged over N sample points is given by

$$\begin{aligned}\Delta^2_{\overline{q'c_s'}} &= \frac{1}{N}\left[\frac{1}{N}\sum_{i=1}^{N}\left(c^2_{s_i'}\Delta^2_{q_i'} + q_i'^2\Delta^2_{c_{s_i}'}\right)\right] \\ &= \frac{1}{N}\left(\Delta^2_{q'}\frac{1}{N}\sum_{i=1}^{N}c^2_{s_i'} + \Delta^2_{c_s'}\frac{1}{N}\sum_{i=1}^{N}q_i'^2\right) \\ &= \frac{1}{N}\left(\Delta^2_{q'}\sigma^2_{c_s'} + \Delta^2_{c_s'}\sigma^2_{q'}\right),\end{aligned} \tag{16}$$

where $\sigma^2_{q'}$ and $\sigma^2_{c_s'}$ are the total variances of the water vapor and sound velocity fluctuations, respectively. A similar analysis for the statistical error of the humidity variance $\overline{q'^2}$ yields

$$\Delta^2_{\overline{q'^2}} = \frac{4}{N}\Delta^2_{q'}\sigma^2_{q'}. \tag{17}$$

In addition, sampling errors have to be taken into account. As described in Lenschow and Stankov (1986), the variance of the time average $c_s'q'$ with respect to the ensemble average is

$$\sigma^2_{\overline{q'c_s'}} = \frac{2(1 + 1/r^2)\,\lambda_{q'c_s'}}{L}\,\overline{c_s'q'}^2, \tag{18}$$

with the correlation coefficient $r = \overline{c_s'q'}(\overline{c_s'^2}\ \overline{q'^2})^{-1/2}$, the integral scale $\lambda_{q'c_s'}$, and the averaging length L. Assuming the validity of Taylor's hypothesis and using Lenschow and Stankov's empirical relation for the integral scale of humidity flux, (18) becomes

$$\sigma^2_{\overline{q'c_s'}} = 0.32\,\frac{(1 + 1/r^2)}{N\delta t\bar{u}}\left(\frac{z}{z_i}\right)^{1/3} z_i\,\overline{c_s'q'}^2, \tag{19}$$

where δt is the time resolution of the c_s' and q' time series and $\bar{u}$ is the average wind speed in the mean wind direction. Similarly, the variance of $\overline{q'^2}$ due to sampling errors is given by

$$\sigma^2_{\overline{q'^2}} = \frac{4}{N\delta t\bar{u}}\left(\frac{z}{z_i}\right)^{1/2} z_i\,\overline{q'^2}^2. \tag{20}$$

The statistical and sampling errors of the latent heat flux E are calculated using (13), (16), (17), (19), and (20).

Figures 7a and 7b show latent heat flux profiles between 450 and 675 m for the following three different measurement intervals:

- Interval 1: 3 h around noon (1136–1436), characterized by rising thermals and entrainment of dry air from the free troposphere.
- Interval 2: 30 min (1315–1345) with strong convection. Cumulus clouds were passing over the measurement site (marked by the arrows in Fig. 3).

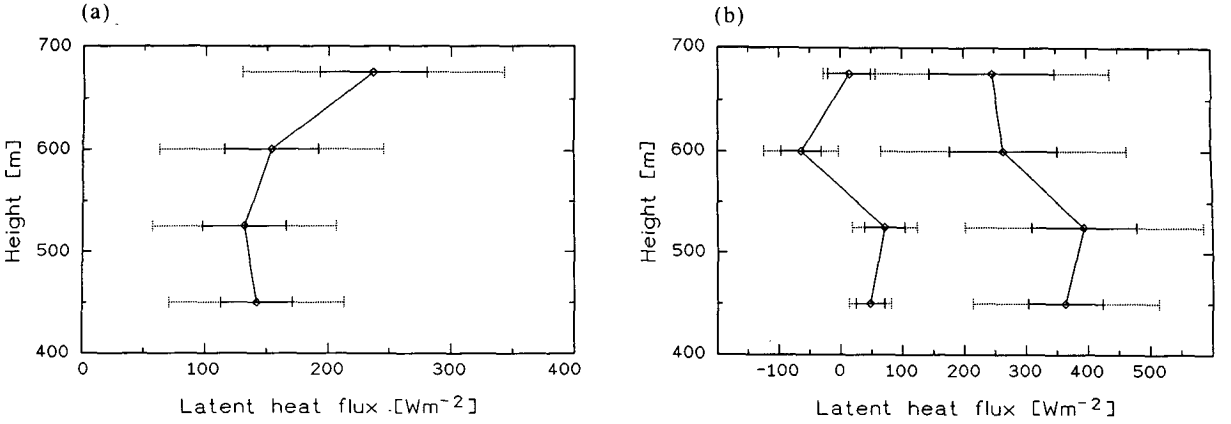

FIG. 7. (a) Latent heat flux profile for measurement interval 1. (b) Latent heat flux profiles for measurement interval 2 (right curve) and 3 (left curve).

- Interval 3: 30 min in the late afternoon (1703–1733), with little convection and no cumulus clouds.

The error bars indicated by solid lines in Figs. 7a and 7b represent the uncertainty of the flux values due to the statistical errors, while the error bars marked by dotted lines indicate the sampling errors. For all cases the sampling errors are about twice as large as the statistical errors. Since the boundary layer is well mixed and the investigated part of the mixed layer contains neither sinks nor sources of water vapor, the water vapor flux profiles are expected to be very close to linear. The scatter of the measured flux values with height can be explained by the statistical errors since the flux measurements for the different heights are independent of each other. A linear regression analysis shows that the errors of the derived vertical flux gradients are too large to obtain any information in addition to the a priori knowledge. This is mainly due to the small height range covered by the instruments in this experiment. It is expected that the height range can be considerably extended in the future, thus allowing significant information about the flux gradients to be obtained. The latent heat fluxes differ considerably for the three measurement intervals, as can be expected from the different meteorological conditions. The water vapor flux measured in the late afternoon after the cumulus clouds dissolved (interval 3) is small with an average value of about 20 W m^{-2}. The flux during interval 2 measured under strongly convective conditions reaches about 320 W m^{-2}, while for interval 1, which encompasses periods of strong convection as well as less turbulent periods, an average flux of about 170 W m^{-2} is found.

Independent measurements of the boundary-layer latent heat flux are not available, but an approximate value of the flux in the middle of the boundary layer can be obtained by estimating surface and entrainment flux and assuming that the water vapor flux changes linearly with height between these two boundary values. The surface latent heat flux is obtained from radiation measurements using the Penman–Monteith model as described in Eq. (3) in De Bruin and Holtslag (1982). Taking the soil heat flux to be 10% of the net radiant flux at the surface and using water vapor measurements at ground-level from the experimental site and typical midlatitude summer values of the atmospheric and surface resistances (De Bruin and Holtslag 1982), the Penman–Monteith model yields an average surface latent heat flux of about 300 W m^{-2} for the first 3 h of the measurement. As can be seen from Fig. 1, during this time interval thermals are penetrating into the free troposphere, and dry air from the free troposphere is entrained downward into the mixed layer causing a positive latent heat flux at the top of the boundary layer. This entrainment flux cannot be estimated reliably from the available data. Latent heat entrainment fluxes measured under similar conditions vary between $0.5(\overline{w'q'})_s$ and $1.5(\overline{w'q'})_s$ (e.g., Stull 1989). Given a surface latent heat flux of about 300 W m^{-2} and an average boundary-layer height of 1200 m (Fig. 1), the latent heat flux at 600 m during the first 3 h of the measurement can be estimated to be between 225 and 375 W m^{-2}. The flux of 170 W m^{-2} measured during interval 1 is lower than this estimate. But taking into account that the measured flux might be underestimated by about 25% due to choosing a filter length of Δt = 30 min and considering the sampling errors of about 90 W m^{-2}, the agreement is reasonable.

5. Conclusions

It has been demonstrated that it is possible to retrieve vertical profiles of water vapor flux in the convective boundary layer with a combination of a ground-based lidar and radar–RASS. In this particular case, the system's time resolution of 60 s was sufficient to resolve the main contributions to the water vapor flux. The simultaneous determination of the instantaneous flux at several height levels is particularly suited to inves-

tigate individual convective flow processes. The system's long-term measurement capability is advantageous for determining the mean turbulent structure of the boundary layer. The statistical significance of the flux measurements can be improved by averaging over a number of similar cases. It is expected that the height range of the DIAL–RASS system can be extended considerably in the future so that a larger portion of the boundary layer can be investigated.

Acknowledgments. This work was supported by the Deutsche Forschungsgemeinschaft.

REFERENCES

Ansmann, A., and J. Bösenberg, 1987: Correction scheme for spectral broadening by Rayleigh scattering in differential absorption lidar measurements of water vapor in the troposphere. *Appl. Opt.*, **26,** 3026–3032.

Bösenberg, J., 1991: A differential absorption lidar system for high resolution water vapor measurements in the troposphere. Max-Planck-Institut für Meteorologie, Report No. 71, Hamburg, Germany. 1–34.

——, and F. A. Theopold, 1988: Evaluation of DIAL measurements in the presence of signal noise. *Proc. 14th Int. Laser Radar Conf.*, San Candido, Italy, 209–211.

Cahen, C., G. Megie, and P. Flamant, 1982: Lidar monitoring of the water vapor cycle in the troposphere. *Appl. Opt.*, **21,** 1506–1515.

Chadwick, R. B., and R. G. Strauch, 1979: Processing of FM–CW Doppler signals from distributed targets. *IEEE Trans. Aerosp. Electron. Syst.*, **15,** 185–189.

De Bruin, H. A. R., and A. A. M. Holtslag, 1982: A simple parameterization of the surface fluxes of sensible and latent heat during daytime compared with the Penman–Monteith concept. *J. Appl. Meteor.*, **21,** 1610–1621.

Harris, C. M., 1971: Effects of humidity on the velocity of sound in air. *J. Acoust. Soc. Amer.*, **49,** 890–893.

Lenschow, D. H., and B. B. Stankov, 1986: Length scales in the convective boundary layer. *J. Atmos. Sci.*, **43,** 1198–1209.

——, J. C. Wyngaard, and W. T. Pennel, 1980: Mean-field and second-moment budgets in a baroclinic, convective boundary layer. *J. Atmos. Sci.*, **37,** 1313–1326.

Peters, G., 1990: Temperature and wind profiles from radar wind profiles equipped with acoustic sources. *Meteor. Rundschau,* **42,** 152–154.

——, and H. J. Kirtzel, 1994: Measurement of the momentum flux in the boundary layer by RASS. *J. Atmos. Oceanic Technol.*, **11,** 63–75.

——, D. Hasselmann, and S. Pang, 1988: Radio acoustic sounding of the atmosphere using a FM–CW radar. *Radio Sci.*, **23,** 640–646.

Schotland, R. M., 1974: Errors in the lidar measurements of atmospheric gases by differential absorption. *J. Appl. Meteor.*, **13,** 71–77.

Stull, R. B., 1976: The energetics of entrainment across a density interface. *J. Atmos. Sci.*, **33,** 1260–1267.

——, 1989: *An Introduction to Boundary Layer Meteorology.* Kluwer Academic, 97 pp.

Taylor, G. I., 1938: The spectrum of turbulence. *Proc. Roy. Soc. London,* **A164,** 476–490.

Webb, E. K., G. I. Pearman, and R. Leuning, 1980: Correction of flux measurements for density effects due to heat and water vapour transfer. *Quart. J. Roy. Meteor. Soc. London,* **106,** 85–100.

Zuev, V. E., Y. S. Makushin, V. N. Marichev, A. A. Mitsel, and V. V. Zuev, 1983: Lidar differential absorption and scattering technique: Theory. *Appl. Opt.*, **22,** 3733–3741.